Evaluation and Correction of B_1^+-Based Brain Subject-Specific SAR Maps Using Electrical Properties Tomography

Jessica A. Martinez 🆔, Alessandro Arduino 🆔, Oriano Bottauscio 🆔, *Senior Member, IEEE*, and Luca Zilberti 🆔

Abstract—The specific absorption rate (SAR) estimates the amount of power absorbed by the tissue and is determined by the electrical conductivity and the E-field. Conductivity can be estimated using Electric Properties Tomography (EPT) but only the E-field component associated with B_1^+ can be deduced from B_1-mapping. Herein, a correction factor was calculated to compensate for the differences between the actual SAR and the one obtained with B_1^+. Numerical simulations were performed for 27 head models at it 128 MHz. Ground-truth local-SAR and 10g-SAR (SAR_{GT}) were computed using the exact electrical conductivity and the E-field. Estimated local-SAR and 10g-SAR (SAR_{EST}) were computed using the electrical conductivity obtained with a convection-reaction EPT and the E-field obtained from B_1^+. Correction factors (CFs) were estimated for gray matter, white matter, and cerebrospinal fluid (CSF). A comparison was performed for different levels of signal-to-noise ratios (SNR). Local-SAR/10g-SAR CF was $3.08 \pm 0/06 / 2.11 \pm 0.04$ for gray matter, $1.79 \pm 0/05 / 2.06 \pm 0.04$ for white matter, and $2.59 \pm 0/05 / 1.95 \pm 0.03$ for CSF. SAR_{EST} without CF were underestimated (ratio across $[\infty - 25]$ SNRs: 0.52 ± 0.02 for local-SAR; 0.55 ± 0.01 for 10g-SAR). After correction, SAR_{EST} was equivalent to SAR_{GT} (ratio across $[\infty - 25]$ SNRs: 0.97 ± 0.02 for local-SAR; 1.06 ± 0.01 for 10g-SAR). SAR maps based on B_1^+ can be corrected with a correction factor to compensate for potential differences between the actual SAR and the SAR calculated with the E-field derived from B_1^+.

Index Terms—Ampère's law, B_1-mapping, electrical conductivity mapping, electrical-properties tomography, head-SAR maps, specific absorption rate.

I. INTRODUCTION

MAGNETIC resonance imaging (MRI) is the preferred imaging modality in the brain [1]. Nonetheless, there are safety concerns about the interactions between the magnetic fields used for imaging and the human body. The interaction of the radio-frequency (RF) field with the human body can result in thermal effects such as localized temperature increases that can cause tissue burning. The increase in temperature is proportional to the amount of power absorbed by the tissue, as measured by the specific absorption rate, SAR (W/kg). As a result, safety standards limit the amount of power applied by the MRI scanner to yield a whole-head SAR to less than 3.2 W/kg [2]. While the whole-head SAR can be below the safety limit, hotspots or regions in which the limit on the local SAR is surpassed can be present, and hence, it is mandatory to find methods to create subject-specific SAR maps during MRI exams.

To obtain head SAR maps, the electrical properties of the tissues and the RF E-field distribution are necessary [3], [4]. Because there is not a straightforward method to characterize the E-field during an MRI examination, SAR maps can be obtained by performing electromagnetic (EM) simulations [5], [6], [7]. The EM simulations usually are performed by modeling clinical RF coils. The coils are often loaded with virtual anatomical models with assigned tissue electrical properties. Subject-specific head EM simulations are not a suitable approach to obtaining head SAR maps during the MRI examination, because they are time-consuming and the electrical properties are unknown.

Conventional MRI techniques can only analyze the information regarding the B_1^+ field. Nonetheless, B_1-based subject-specific SAR maps have been proposed [8], [9], [10]. As regards the electrical properties, one possible way to obtain them is electrical properties tomography (EPT) [11], [12]. EPT is an emerging quantitative technique that enables the non-invasive characterization of electrical properties (EPs) at the frequency of interest. The electrical conductivity, necessary for obtaining SAR quantification, can be obtained from the phase information of the B_1^+ field. The E-field, on the other hand, can be obtained by applying Ampère's law to the B_1 field, assuming a unit relative magnetic permeability throughout the investigated tissues and the electric properties estimated by EPT.

The circularly polarized B_1-field can be separated into three main components: B_1^+, which is responsible to tip the magnetization into the transverse plane; B_1^-, which rotates in the opposite direction to B_1^+ and has no role in the image acquisition but interacts with the tissues as energy deposition; and the longitudinal $B_{1,z}$ [13]. B_1- mapping techniques can only measure B_1^+. Thus, it is not possible to obtain the whole EM profile, since the E-field depends on all components, including B_1^- and $B_{1,z}$ [14]. Thus, calculating the E-field using only B_1^+ may misrepresent the true E-field. Previous works have demonstrated that, usually, B_1^+ is the dominant component of the B_1 field during MRI [10], [13], but the remaining components are needed to obtain an accurate estimate of SAR. To this

day it is still unknown if B_1^+-based SAR can be corrected or modified to compensate for the missing components. Therefore, the objective of this work is to evaluate subject-specific head SAR maps derived only from the information given by the B_1^+ field and the existing EPT techniques. In addition, a correction factor was calculated and implemented to compensate for the missing E-field information.

II. METHODS

Subject-specific SAR maps were obtained, through numerical simulations, for twenty-seven heterogeneous whole-head human models with the electrical properties provided by [15] (8 from the Virtual Population of the IT'IS Foundation [16], 19 from the XCAT library [17], 11 male/16 female, mean [standard deviation, SD] age, and BMI were 23.8 [20.4] years and 20.7 [6.5] kg m^{-2}, respectively). The features of these models are summarized in supplemental Table I.

Electric and B_1^+ fields per model were generated from numerical simulations performed at the frequency of 128 MHz, using the FEM-BEM code described in [18]. The models were placed in an MRI birdcage coil with the center of their heads placed at the isocenter. The coil was used in transmission and reception and consisted of a 16-leg body coil (radius 35 cm, height 45 cm) simulated as current-driven (in each leg we put an ideal current of amplitude equal to 1 A and properly phase-shifted). The human models were discretized to simulate field maps with a 2 mm resolution.

For each model, voxel-wise SAR maps were obtained (local-SAR), where analysis of median values was performed. To analyze the distribution of the maximum obtained values, and to comply with the safety standards, 10g-SAR maps were also acquired [2]. Both local-SAR and 10g-SAR maps were analyzed for the 30 transverse slices that covered the center region of the models' brains.

A. Electrical Conductivity Based on EPT

Voxel-wise reconstructed electrical conductivity values were obtained from the phase of B_1^+ using the convection-reaction EPT (CR-EPT) approach implemented in EPTlib [19], [20]. For all the models, the reconstruction was performed using a three-dimensional cross-shaped Savitzky-Golay filter with size (1,1,1, 7 voxels in total), Dirichlet boundary condition of 0.1 S/m, and artificial diffusion coefficient of 0.001 rd. Since, in general, the accuracy of EPT reconstructions for permittivity is significantly lower than the accuracy achievable for conductivity, permittivity was not estimated via EPT.

B. SAR Estimation

For the twenty-seven models, under the assumption of a tissue density of 1000 kg m^{-3}, two sets of SAR maps were calculated. The first set corresponded to the ground-truth SAR (SAR$_{GT}$), which was computed using the exact tissue electrical conductivity and electrical permittivity and the total E-field obtained from simulations. The second set corresponded to the estimated SAR (SAR$_{EST}$), computed using the exact tissue
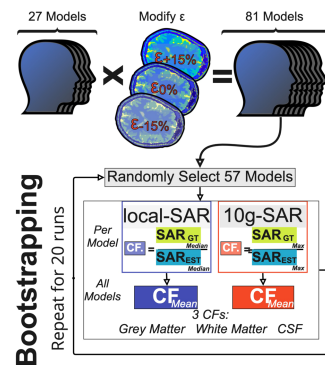

Fig. 1. Bootstrapping workflow used to calculate the correction factor and repeated 20 times. The correction factor was calculated by dividing the SAR$_{GT}$ and SAR$_{EST}$ values. For local-SAR (blue), the correction factor was obtained using the global median values. Whereas for 10g-SAR (red), the correction factor was obtained using the global maximum values. Two sets of correction factors (local-SAR and 10g-SAR) were obtained for gray matter, white matter, and CSF.

electrical permittivity, the EPT-based electrical conductivity, and the E-field derived by numerically solving Ampère's law using finite differences on B_1^+ only following [21]. The estimated E-field was then filtered using a 2-D boundary-based median filter [22] (size = 9) to reduce noise propagated by the finite differences.

C. 10g-SAR Estimation

10-gram SAR maps were also calculated since they can be potentially translated as temperature increases in hot-spot regions. The 10-gram SAR maps were obtained by averaging the (SAR$_{GT}$) and (SAR$_{EST}$) values in a cube of 10 cm^3, assuming that the tissue density is 1000 kg m^{-3}. When air was present in the averaging cube, the computation was not performed. The averaged value was assigned to the voxel in the center of the cube. To minimize an overestimation of the 10g-SAR, and to avoid eliminating information regarding potential hotspots, outlier values were excluded from the analysis. To do so, prior to the 10g-SAR calculation, a z-score-based outlier reduction was performed considering all the voxels within the whole head, without tissue segmentation. This led to the removal of the voxels where local-SAR values were greater than the mean plus 7 standard deviations. Such voxels were considered as made of air. Thus, 10g-SAR maps were obtained starting from 99.99% of the local-SAR data.

D. Estimation of the Correction Factor

The correction factor (CF) was calculated independently of the spatial location. Thus, the estimation of the CF was performed for three tissues: gray matter, white matter, and CSF. Each CF corresponded to the ratio between SAR$_{GT}$ and SAR$_{EST}$ and was obtained using a bootstrapping approach [23], as presented in Fig. 1. The bootstrapping workflow was as follows: per each bootstrapping run, 70% of the models were randomly selected from the pool. From this cohort group, SAR$_{GT}$ and SAR$_{EST}$ noiseless values were calculated and the ratio between the overall values (mean and maximum) was performed.

The bootstrapping was repeated 20 times and the global average value between runs was reported as the CF per tissue. The estimation of the permittivity using EPT techniques is yet not as robust as that of the conductivity [24]. Herein, the permittivity of each tissue was assigned based on literature (i.e., equal to the exact value adopted in the simulations). However, in order to account for possible electrical permittivity estimation errors, when calculating SAR_{EST}, the permittivity was also varied for each model with an additive correction of -15%, 0 and $+15\%$. These led to the creation of a pool of 81 models. From this model pool, noiseless local-SAR and 10g-SAR maps were calculated with a subset of 57 models randomly selected to estimate the CF.%

Prior to obtaining the CF per tissue, the SAR maps were segmented following the perfect segmentation provided by the simulation software. The local-SAR CF per tissue was obtained, for each model, by dividing the global median ground-truth value by the global median estimated value. The 10g-SAR CF was obtained by dividing the global maximum ground-truth value by the global maximum estimated value (it is worth noting that, in general, the two values used in this calculation may correspond to different voxels). The CFs obtained for both local-SAR and 10g-SAR were calculated by averaging the CFs computed for the 20 runs. In turn, the CF of each run was obtained as the mean value between those calculated for the 57 considered models.

E. Noise Analysis

To test the feasibility of the CF implementation in realistic settings, the electrical conductivity, local-SAR, and 10g-SAR were calculated with noisy data. To do so, complex Gaussian noise was added to B_1^+ at five different SNR levels (∞, 150, 50, 25, 10). The B_1^+ distribution was filtered with a Gaussian filter (with unit standard deviation) before performing the analysis. After denoising, local-SAR and 10g-SAR values were corrected with the CF previously calculated. For all noise levels, local-SAR values were compared by analyzing the median local-SAR_{GT} and local-SAR_{EST} values. Similarly, 10g-SAR values were compared by analyzing the 10g-SAR_{GT} and 10g-SAR_{EST} maximum values. The relative change of corrected SAR_{EST} to SAR_{GT} greater than 25% was considered substantial.

Local-SAR and 10g-SAR voxel-wise approximation error analysis was performed by analyzing the relative error between SAR_{GT} and SAR_{EST} for all noise levels. The relative error was computed by the absolute difference of the SAR_{GT} and SAR_{EST} divided by the SAR_{GT}.

III. RESULTS

To illustrate the local-SAR underestimation dependence due to the estimated E-field, electrical conductivity and permittivity, a comparison of the distribution of global median local-SAR_{GT} to noiseless local-SAR_{EST} was performed (Fig. 2) for three cases: i) with exact E-field but with the electrical conductivity obtained via CR-EPT; ii) with exact electrical conductivity and the E-field estimated from B_1^+, and iii) with electrical conductivity obtained via CR-EPT and the E-field estimated from B_1^+. For the first case (Fig. 2(a)), local-SAR_{EST} resulted in a similar
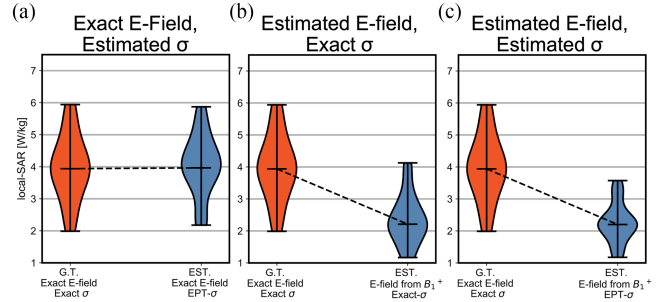

Fig. 2. Median local-SAR_{GT} and local-SAR_{EST} calculated using the exact E-field and conductivity estimated using a CR-EPT approach (a), the E-field obtained from B_1^+ and the exact conductivity (b) and the E-field obtained from B_1^+ and the conductivity estimated using a CR-EPT approach (c). The underestimation was mostly due to the use of the E-field derived from the B_1^+ field only.
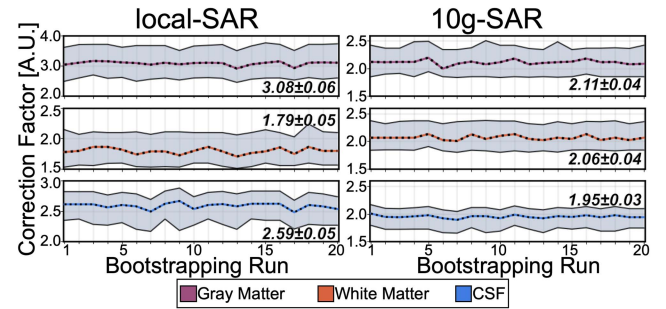

Fig. 3. Correction Factor for local-SAR and 10g-SAR maps for gray matter, white matter, and CSF with respect to bootstrapping run. (**Note:**) y-axis limit differ from each plot.

distribution compared to local-SAR_{GT} (EST: (3.84 ± 0.92) W/kg; GT: (3.94 ± 1.02) W/kg). Local-SAR_{EST} for the second and third cases (Fig. 2(b) and (c)), resulted in lower values compared to local-SAR_{GT}. However, the resulting values between these two cases were equivalent (EST-exact conductivity: (2.36 ± 0.73) W/kg; EST-estimated conductivity: (2.26 ± 0.58) W/kg). Example qualitative maps of the E-field and the electrical conductivity distributions are shown in the supplemental Fig. 1.

Fig. 3 shows the values of the CF for local-SAR and 10g-SAR calculated for gray matter, white matter, and CSF per bootstrapping run, evaluated on noiseless data. The random selection of the models did not affect the evaluation of the CF per bootstrapping run, suggesting its reliability. The local-SAR CF was 3.08 ± 0.06 for gray matter, 1.79 ± 0.05 for white matter, and 2.59 ± 0.05 for CSF. Whereas the 10g-SAR CF was 2.11 ± 0.04 for gray matter, 2.06 ± 0.04 for white matter, and 1.95 ± 0.03 for CSF.

Local-SAR and 10g-SAR voxel-wise distributions for the SAR_{EST} with respect to SAR_{GT} for all models and all target tissues at all noise levels are shown in Fig. 4. Values without CF were observed to be underestimated (across $[\infty - 25]$ SNR, the ratio resulted to be 0.52 ± 0.02 for local-SAR and 0.55 ± 0.01 for 10g-SAR). However, after the multiplication by the CF, SAR_{EST} was equivalent to SAR_{GT} (across $[\infty - 25]$ SNR, the ratio resulted being 1.15 ± 0.02 for local-SAR and 1.09 ± 0.05 for 10g-SAR). At very low SNR the added noise levels
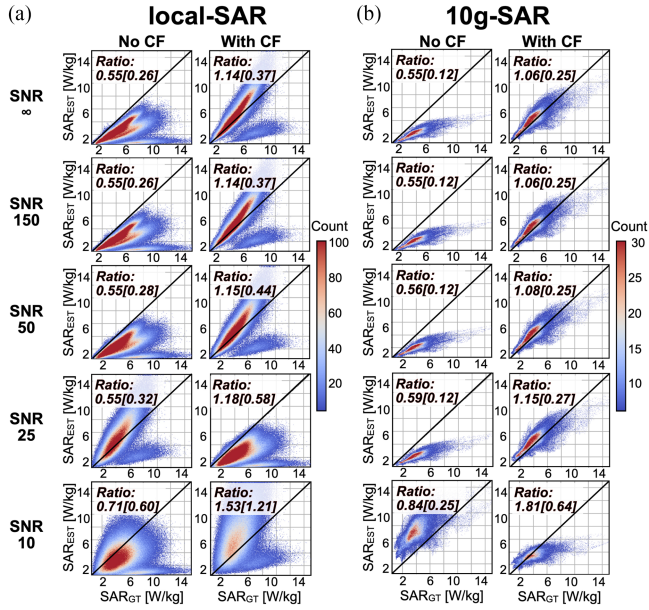
Fig. 4. Voxel-wise 2-D distribution of the local-SAR (a) and 10g-SAR (b) maps at all SNR levels. Values without correction factor (left column), were underestimated. In most voxels, the underestimation got resolved by using a correction factor (right column). **Note**: colorbar refers to the number of voxels that fall within the same SAR range.
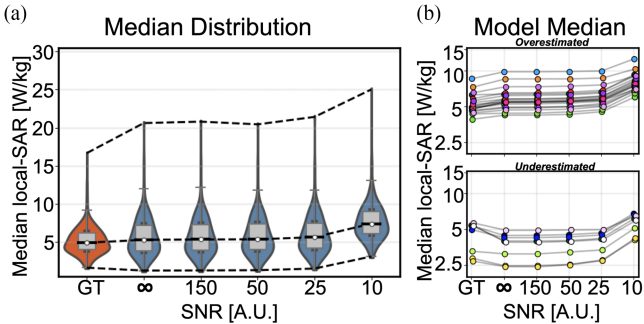

Fig. 5. Local-SAR median value distribution for the SAR_{GT} (red) and the corrected SAR_{EST} (blue) at all SNR values. (a) Violin plots corresponding to the median value distribution for all slices and all models. (b) Scatter plot corresponding to the overall median value per model represented with different colors (logarithmic y-axis). Out of the 27 models, only 2 models resulted in underestimated median local-SAR of more than 25% after correction.

impacted the SAR_{EST}. For SNR of 10, the ratio of SAR_{EST} to SAR_{GT} was 0.75 without correction and 1.53 after correction for local-SAR; 0.71 without correction and 1.81 after correction for 10g-SAR. Certain voxels on the local-SAR_{EST} distribution resulted in lower estimation values compared to local-SAR_{GT}, generating an additional clustering of values. This clustering resulted from the aggregation of local-SAR outliers observed across all models, tissues, and slices (supplemental Fig. 2). However, this underestimation did not affect the overall local-SAR distribution.

Median local-SAR values evaluated for each slice of each model (considering the three target tissues together) are shown in Fig. 5. The distribution of median corrected local-SAR_{EST} values per slice (Fig. 5(a)) at SNR levels greater than 10 agree with the median local-SAR_{GT} values. Similar results were observed
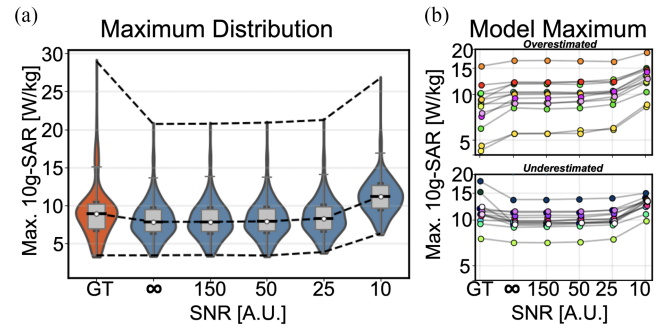

Fig. 6. 10g-SAR maximum distribution analysis for the SAR_{GT} (red) and the corrected SAR_{EST} (blue) at all SNR values. (a) Violin plots corresponding to the maximum value distribution for all slices and all models. (b) Scatter plot corresponding to the overall maximum value per model represented with different colors (logarithmic y-axis).

TABLE I
MEAN RELATIVE ERROR VALUES BETWEEN SAR_{EST} AND THE SAR_{GT} AT DIFFERENT SNR LEVELS FOR ALL MODELS

local-SAR [mean (SD)]				
SNR ∞	SNR 150	SNR 50	SNR 25	SNR 10
0.09 (0.10)	0.09 (0.09)	0.09 (0.09)	0.10 (0.07)	0.35 (0.14)

10g-SAR [mean (SD)]				
SNR ∞	SNR 150	SNR 50	SNR 25	SNR 10
0.09 (0.05)	0.09 (0.05)	0.09 (0.05)	0.12 (0.01)	0.57 (0.14)

for the overall local-SAR median values per model (Fig. 5(b)). Out of the 27 models, only 2 models resulted in underestimated median local-SAR of more than 25% after correction. For an SNR of 10, the noise affected the resultant values, thus the median corrected local-SAR_{EST} values were overestimated by more than 25% for 22 models compared to the SAR_{GT}.

10g-SAR maximum value distribution for all models and all slices and model global maximum values are shown in Fig. 6. On the whole, the distribution of maximum corrected 10g-SAR_{EST} values obtained for all models at all slices (Fig. 6(a)) agreed with 10g-SAR_{GT}. For six models, global maxima were still affected by an underestimation larger than 25% after correction (Fig. 6(b)).

Mean relative error values between SAR_{EST} and the SAR_{GT} at different SNR levels are shown in Table I. For SNR levels greater than 10, SAR_{EST} showed a good agreement with respect to SAR_{GT} (relative error: 0.09 $\pm$ 0.10 for local-SAR; 0.09 $\pm$ 0.05 for 10g-SAR). Regions with low SAR_{EST} values presented a greater relative error compared to regions with high SAR_{EST} values.

Fig. 7 shows single model qualitative local-SAR and 10g-SAR maps before and after applying the CFs and their respective relative error maps at different SNR levels. Before applying the CF, the local-SAR and 10g-SAR maps were underestimated. After applying the CF, the map distributions were similar to the GT for SNR levels between 150-25. For an SNR of 10,
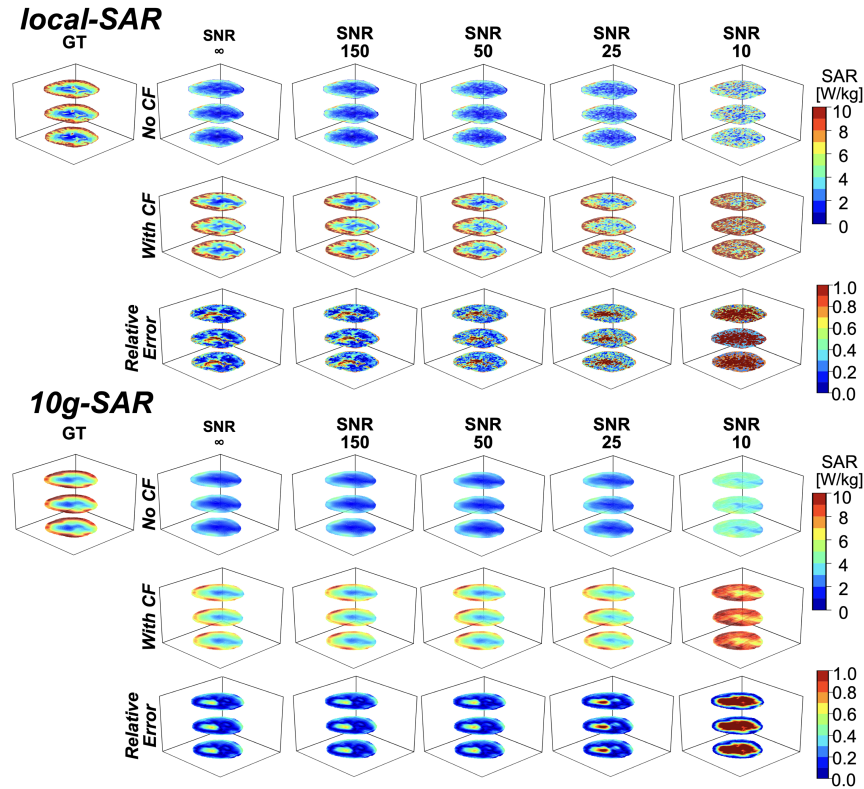
Fig. 7. Local-SAR and 10g-SAR maps of a single model for the SAR_{GT} and SAR_{EST} before correction factor (No CF) and after correction factor (with CF) and the relative error. For SNR greater than 25, SAR_{EST} with the proposed correction factors resulted in a similar SAR distribution to SAR_{GT}.

the obtained SAR maps were affected by the noise and the estimation was not accurate.

IV. DISCUSSION

The interaction between the RF field and the human head during neurological MRI examinations is still a safety concern. The amount of energy absorbed by the head can be analyzed via subject-specific SAR mapping. To calculate reliable SAR maps, it is necessary to accurately estimate the electrical properties (EPs) of the tissues and the distribution of the RF E-field in the region of interest.

Traditionally, SAR maps are obtained using numerical simulations that often use virtual models with EPs values previously reported in literature [5]. These simulations are the gold standard of SAR analysis since they enable a voxel-wise characterization of the E-field. Because subject-specific numerical simulations can be time-consuming, this implementation is not suitable to be used during an MRI examination. Thus, it is necessary to obtain SAR maps from the information provided by existing MRI sequences.

The SAR method evaluated herein allows obtaining reasonable head SAR maps from information that can be derived from MR-based B_1-mapping techniques. From the obtained B_1 fields, the EPs can be calculated with the existing EPT techniques, such as the CR-EPT, and the E-field can be resolved by solving Ampère's law. Nonetheless, the available MR-based

B_1-mapping techniques can only measure the B_1^+ component of the field. This has no bearing on estimating electrical conductivity because CR-EPT can perform analyses only with the phase information of the B_1^+. However, to correctly estimate the E-field distribution, it is necessary to know B_1^- and $B_{1,z}$. While methods for calculating B_1^- have been proposed [25], the implementation in clinical settings can be challenging, leaving the estimation of subject-specific head SAR estimation with the B_1^+ field as the only available method.

Different methods have estimated subject-specific SAR maps during MRI exams, based on an equivalent circuit model [26], using hybrid simulation and data acquisition approaches [27], or like in this work, using B_1 fields [28], [29]. The B_1^+ approaches, however, have not compared the SAR obtained with the whole B_1 to the SAR obtained with B_1^+ only. Herein, B_1^+-based head SAR maps were also calculated, and the electrical conductivity was estimated using a phase-based CR-EPT approach (SAR_{EST}). Compared to the SAR maps calculated with the whole component of the E-field and the true electrical conductivity (SAR_{GT}), the resultant SAR_{EST} maps were misestimated. Subject-specific head SAR maps using only B_1^+ have also been previously investigated numerically at 3T [30]. Similar to the results obtained herein, underestimated SAR maps were obtained when neglecting B_1^- and $B_{1,z}$.

Here, a correction factor (CF) has been proposed to compensate for the possible head SAR misestimation values. Because the electrical properties will affect SAR, the CF was calculated

from a pool of 81 models that corresponded to a combination of electrical conductivity obtained from CR-EPT and with the electrical permittivity varied with additive corrections. These permittivity variations were chosen mostly because the existing EPT techniques are still not accurate enough to obtain reliable permittivity values. Nonetheless, the knowledge of the average permittivity of biological tissues within the population is provided by databases [15] and can be assumed to vary in healthy subjects with a dispersion of $\pm 15\%$, thus the same variability was implemented in this study. The CF was calculated using healthy models of varying ages, including pediatric models. This was done to account for different body shapes on the CF estimation. However, no change in EPs variability due to the model's age was included in this work. To accurately correct the head SAR maps, a segmentation strategy was performed. The SAR maps were segmented into gray matter, white matter, and CSF, and three CFs were obtained for each tissue following a bootstrapping approach. Herein, the segmentation was provided by the numerical simulation software. However, several segmentation strategies have been proposed [31] and can be applied both offline and during an MRI examination [32].

The feasibility of the CF to obtain accurate head SAR maps was tested on twenty-seven virtual models at different SNR values. The analysis was performed for local-SAR maps and 10g-SAR maps. 10g-SAR maps can be used to analyze potential temperature increases in hot-spot regions [33]. Additionally, to further evaluate the impact of noise, head SAR maps were obtained and corrected at different SNR values. Before calculating the SAR maps, Gaussian noise was added to the B_1^+ data and a Gaussian filter was applied. While an underestimation was observed in some voxels of the local-SAR$_{EST}$, possibly due to errors related to each step applied for estimating SAR, corrected median local-SAR$_{EST}$ values agreed with local-SAR$_{GT}$ values for SNR levels greater than 10 for all the analyzed models. The upper-threshold 10g-SAR maps yielded similar results. The maximum corrected 10g-SAR$_{EST}$ values obtained for some models, however, were lower than the maximum 10g-SAR$_{GT}$. Maximum 10g-SAR values are expected to occur at the brain boundaries [34]. Therefore, the Gaussian filtering performed on the B_1^+ before calculating SAR$_{EST}$ may have resulted in these voxel values being left out of the analysis, resulting in a potential underestimation of hotspots. A greater relative error was observed in regions where SAR is expected to be the lowest, this is mostly because the proposed correction factor is spatially constant. However, from a safety perspective, without the presence of implants, in the expected low-SAR regions, low heating risks are expected [35]. In the regions where SAR is expected to be the greatest and thus should be monitored during an MRI examination, the relative error was the lowest.

It must be finally noted that, in this first attempt to get a subject-specific SAR evaluation, the CF was derived starting from a quite heterogeneous population of human models, which might have complicated the correction process. The use of a larger population, in which the human models are grouped based on their features (e.g. age and BMI), could allow obtaining more specific values of the CF, optimized for the application on a given phenotype.

V. LIMITATIONS

This work has some limitations that must be pointed out. Firstly, a constant tissue mass density of 1000 kg m^{-3} was used. This was done assuming that the tissue characteristics are not known a priori and because information regarding the tissue density cannot be obtained with traditional MR methods. In this work, a CF has been proposed for the white matter, gray matter, and CSF. Thus, it is mandatory to use a segmentation technique to correct SAR, and therefore, it is possible to assign a non-constant tissue density from the literature. Nonetheless, a small error is expected since the density of white matter, gray matter, and CSF are within the same range as the density of water [15], [36].

Secondly, the presented SAR estimation is based on the information given by the B_1^+ fields that can be obtained with MRI. The fields used herein were derived from numerical simulations in which the information is obtained in ideal scenarios. In this work, Gaussian noise was added and resolved before estimating SAR. However, in realistic settings, the B_1^+ field estimation may be perturbed by several external factors such as B_0 inhomogeneity and off-resonance effects. Thus, an experimental feasibility study (with phantoms or in vivo) that combines the acquisition of B_1^+ data along with a numerical simulation framework for analyzing the resultant SAR maps and the proposed CFs is necessary.

Thirdly, this work only investigated subject-specific SAR maps in clinical scanners where the transceive phase assumption is applicable (≤ 3 T) [37]. At greater field strengths, such as 7 T, patient-specific SAR analysis following the proposed approach may not be applicable. Future work must analyze the feasibility to estimate the electrical conductivity and SAR maps using multi-transmit RF coils at 7 T.

Lastly, SAR maps can benefit the safety assessment of patients with implanted devices during an MRI examination. In this work, device-free maps were obtained. Future work needs to be performed to check if the work proposed here can be applied to identifying potential hotspots due to the interactions between the RF field and the implanted device, taking into account that the presence of a metallic implant could induce image artifacts.

VI. CONCLUSION

This work demonstrates that local and 10-gram SAR maps can be generated from B_1^+ data. A CF was proposed to compensate for the potential differences between the SAR calculated with the whole E-field and the SAR calculated with the E-field derived from B_1^+. The estimation of the CF was thought to potentially correct subject-specific SAR maps during MRI examinations. Thus, the CF was simplified to be tissue-related rather than voxel location-related. Future work will focus on calculating a CF according to population characteristics (age, gender BMI), validating the CF in vitro, and testing the applicability of subject-specific SAR maps in vivo.

References

[1] W. Mier and D. Mier, "Advantages in functional imaging of the brain," *Front. Hum. Neurosci.*, vol. 9, 2015, Art. no. 249.

[2] *Medical Electrical Equipment Part 2–33: Particular Requirements for the Basic Safety and Essential Performance of Magnetic Resonance Equipment for Medical Diagnosis,* IEC 60601-2-33 G:2018 AMD1:2013 AMD2: 2015 CSV, IEC Standard, 2018.

[3] L. P. Panych and B. Madore, "The physics of MRI safety," *J. Magn. Reson. Imag.*, vol. 47, no. 1, pp. 28–43, 2018.

[4] W. D. Hurt, J. M. Ziriax, and P. A. Mason, "Variability in EMF permittivity values: Implications for SAR calculations," *IEEE Trans. Biomed. Eng.*, vol. 47, no. 3, pp. 396–401, Mar. 2000.

[5] D. J. Panagopoulos, O. Johansson, and G. L. Carlo, "Evaluation of specific absorption rate as a dosimetric quantity for electromagnetic fields bioeffects," *PLoS One*, vol. 8, no. 6, 2013, Art. no. e62663.

[6] L. Alon, C. M. Deniz, G. Carluccio, R. Brown, D. K. Sodickson, and C. M. Collins, "Effects of anatomical differences on electromagnetic fields, SAR, and temperature change," *Concepts Magn. Reson. Part B, Magn. Reson. Eng.*, vol. 46, no. 1, pp. 8–18, 2016.

[7] N. Gurler and Y. Z. Ider, "Numerical methods and software tools for simulation, design, and resonant mode analysis of radio frequency birdcage coils used in MRI," *Concepts Magn. Reson. Part B, Magn. Reson. Eng.*, vol. 45, no. 1, pp. 13–32, 2015.

[8] H. Homann, P. Börnert, H. Eggers, K. Nehrke, O. Dössel, and I. Graesslin, "Toward individualized SAR models and in vivo validation," *Magn. Reson. Med.*, vol. 66, no. 6, pp. 1767–1776, 2011.

[9] E. Balidemaj et al., "B_1-based SAR reconstruction using contrast source inversion–electric properties tomography (CSI-EPT)," *Med. Biol. Eng. Comput.*, vol. 55, no. 2, pp. 225–233, 2017.

[10] U. Katscher, T. Voigt, C. Findeklee, P. Vernickel, K. Nehrke, and O. Doessel, "Determination of electric conductivity and local SAR via B_1 mapping," *IEEE Trans. Med. Imag.*, vol. 28, no. 9, pp. 1365–1374, Sep. 2009.

[11] X. Zhang, J. Liu, and B. He, "Magnetic-resonance-based electrical properties tomography: A review," *IEEE Rev. Biomed. Eng.*, vol. 7, pp. 87–96, 2014.

[12] J. Liu, Y. Wang, U. Katscher, and B. He, "Electrical properties tomography based on B_1 maps in MRI: Principles, applications, and challenges," *IEEE Trans. Biomed. Eng.*, vol. 64, no. 11, pp. 2515–2530, Nov. 2017.

[13] M. V. Vaidya, C. M. Collins, D. K. Sodickson, R. Brown, G. C. Wiggins, and R. Lattanzi, "Dependence of and field patterns of surface coils on the electrical properties of the sample and the MR operating frequency," *Concepts Magn. Reson. Part B: Magn. Reson. Eng.*, vol. 46, no. 1, pp. 25–40, 2016.

[14] T. S. Ibrahim, Y.-K. Hue, and L. Tang, "Understanding and manipulating the RF fields at high field MRI," *NMR Biomed., Int. J. Devoted Develop. Appl. Magn. Reson. In vivo*, vol. 22, no. 9, pp. 927–936, 2009.

[15] P. Hasgall et al., "IT'IS database for thermal and electromagnetic parameters of biological tissues, Version 4.0," Foundation for Research on Information Technologies in Society, Zürich, Switzerland, 2018. [Online]. Available: https://itis.swiss/virtual-population/tissue-properties/downloads/database-v4-0/

[16] A. Christ et al., "The Virtual Family–development of surface-based anatomical models of two adults and two children for dosimetric simulations," *Phys. Med. Biol.*, vol. 55, no. 2, 2009, Art. no. N23.

[17] W. P. Segars, B. M. Tsui, J. Cai, F.-F. Yin, G. S. Fung, and E. Samei, "Application of the 4-D XCAT phantoms in biomedical imaging and beyond," *IEEE Trans. Med. Imag.*, vol. 37, no. 3, pp. 680–692, Mar. 2018.

[18] O. Bottauscio, M. Chiampi, and L. Zilberti, "Massively parallelized boundary element simulation of voxel-based human models exposed to MRI fields," *IEEE Trans. Magn.*, vol. 50, no. 2, pp. 1029–1032, Feb. 2014.

[19] A. Arduino, "EPTlib: An open-source extensible collection of electric properties tomography techniques," *Appl. Sci.*, vol. 11, no. 7, 2021, Art. no. 3237.

[20] A. Arduino, "EPTlib v0.3.1," INRiM 2022. [Online]. Available: https://eptlib.github.io/

[21] J. Chen, Z. Feng, and J.-M. Jin, "Numerical simulation of SAR and B_1-field inhomogeneity of shielded RF coils loaded with the human head," *IEEE Trans. Biomed. Eng.*, vol. 45, no. 5, pp. 650–659, May 1998.

[22] M. Sarvesh, M. Sivagami, and N. Maheswari, "Removal of noise in an image using boundary detection technique," *J. Phys., Conf. Ser.*, vol. 1911, no. 1, 2021, Art. no. 012018.

[23] B. EFRON, "Bootstrap methods: Another look at the Jacknife," *Ann. Stat.*, vol. 7, pp. 1–26, 1979.

[24] S. Gavazzi et al., "Accuracy and precision of electrical permittivity mapping at 3T: The impact of three mapping techniques," *Magn. Reson. Med.*, vol. 81, no. 6, pp. 3628–3642, 2019.

[25] J. Wang, M. Qiu, Q. X. Yang, M. B. Smith, and R. T. Constable, "Measurement and correction of transmitter and receiver induced nonuniformities in vivo," *Magn. Reson. Med.*, vol. 53, no. 2, pp. 408–417, 2005.

[26] W. Jiang, F. Yang, and K. Wang, "Individualized and accurate SAR characterization method based on equivalent circuit model for MRI system," *Magn. Reson. Med.*, vol. 87, no. 6, pp. 2997–3010, 2022.

[27] E. Milshteyn et al., "Individualized SAR calculations using computer vision-based MR segmentation and a fast electromagnetic solver," *Magn. Reson. Med.*, vol. 85, no. 1, pp. 429–443, 2021.

[28] M. Cloos, "Towards direct B_1 based local SAR estimation," in *Proc Int. Soc. Mag. Reson. Med.*, vol. 17, 2009, Art. no. 3037.

[29] T. Voigt, U. Katscher, and O. Doessel, "Quantitative conductivity and permittivity imaging of the human brain using electric properties tomography," *Magn. Reson. Med.*, vol. 66, no. 2, pp. 456–466, 2011.

[30] T. Voigt, H. Homann, U. Katscher, and O. Doessel, "Patient-individual local SAR determination: In vivo measurements and numerical validation," *Magn. Reson. Med.*, vol. 68, no. 4, pp. 1117–1126, 2012.

[31] C. Velasco-Annis, A. Akhondi-Asl, A. Stamm, and S. K. Warfield, "Reproducibility of brain MRI segmentation algorithms: Empirical comparison of local MAP PSTAPLE, freesurfer, and FSL-FIRST," *J. Neuroimag.*, vol. 28, no. 2, pp. 162–172, 2018.

[32] D. Lyell, E. Coiera, J. Chen, P. Shah, and F. Magrabi, "How machine learning is embedded to support clinician decision making: An analysis of FDA-approved medical devices," *BMJ Health Care Informat.*, vol. 28, no. 1, 2021, Art. no. e100301.

[33] F. Adibzadeh, M. M. Paulides, and G. C. van Rhoon, "SAR thresholds for electromagnetic exposure using functional thermal dose limits," *Int. J. Hyperthermia*, vol. 34, no. 8, pp. 1248–1254, 2018.

[34] T. M. Fiedler, M. E. Ladd, and A. K. Bitz, "SAR simulations & safety," *Neuroimage*, vol. 168, pp. 33–58, 2018.

[35] P. Nordbeck et al., "Spatial distribution of RF-induced E-fields and implant heating in MRI," *Magn. Reson. Med., Official J. Int. Soc. Magn. Reson. Med.*, vol. 60, no. 2, pp. 312–319, 2008.

[36] C. Gabriel, "Compilation of the dielectric properties of body tissues at RF and microwave frequencies," Dept. of Physics, King's Coll London, U.K., Tech. Rep. AFOSR-TR-96-0135, 1996.

[37] A. L. van Lier et al., "Electrical properties tomography in the human brain at 1.5, 3, and 7T: A comparison study," *Magn. Reson. Med.*, vol. 71, no. 1, pp. 354–363, 2014.

Jessica A. Martinez received the Ph.D. degree in bioengineering in 2019 from the University of California Los Angeles, Los Angeles, CA, USA. Since 2021, she has been with the Istituto Nazionale di Ricerca Metrologica, Turin, Italy, where she is a Postdoctoral Researcher. Her research interests include MRI safety, quantitative MRI, electromagnetic tissue properties, and electromagnetic dosimetry focused on biomedical and clinical applications.

Alessandro Arduino received the B.Sc. degree in mathematics for engineering sciences, the M.Sc. degree in mathematical engineering, and the Ph.D. degree in electrical, electronics, and communications engineering from the Politecnico di Torino, Turin, Italy, in 2012, 2014, and 2018, respectively. Since 2018, he has been with the Istituto Nazionale di Ricerca Metrologica, Turin, Italy. He is the maintainer of EPTlib, an open-source C++ library of electric properties tomography methods. His research interests include mathematical and numerical modeling of electromagnetism applied to biomedical engineering and inverse problems.

Oriano Bottauscio (Senior Member, IEEE) is currently the Research Director with the Istituto Nazionale di Ricerca Metrologica (INRIM), Turin, Italy. He has authored or coauthored around 250 scientific papers, with more than 2300 citations and h-index equal to 23 (source: Scopus). He is the Deputy Coordinator of the Ph.D. School in Metrology, held by Politecnico di Torino, Turin, Italy, in convention with INRIM. From 1996 to 2001, he was a Contract Professor with Politecnico di Torino in electrical engineering. His research activities include computational electromagnetism, with main reference to bioelectromagnetics, electromagnetic dosimetry related to medical equipment, electromagnetic fields and human exposure. He was an Associate Editor (in 2009 and 2011) and Chief Editor (in 2013) of the special issues of the IEEE TRANSACTIONS ON MAGNETICS related to the Soft Magnetic Materials Conference. He was responsible for and participated in several national and European research projects. He has been a Member of CENELEC TC 106X Electromagnetic field in human environment-WG3 Measurement and calculation procedures in electric, magnetic, and electromagnetic fields (0 Hz-300 GHz) and of the CIGRE Task Force C4.204 Magnetic Field Mitigation Techniques.

Luca Zilberti received the B.S., M.S., and Ph.D. degrees in electrical engineering from the Politecnico di Torino, Turin, Italy, in 2004, 2006, and 2010, respectively. Since 2010, he has been with the Istituto Nazionale di Ricerca Metrologica, Turin. His research interests include electromagnetic field theory and the modeling of electromagnetic phenomena, with particular reference to the development of computational methods for electromagnetic dosimetry and the biomedical application of electromagnetic fields. Dr. Zilberti was the recipient of the Young Scientist Award from the International Commission on Non-Ionizing Radiation Protection. He is the Coordinator of the European EMPIR Project 18HLT05 Quantitative MR-based imaging of physical biomarkers.